2013

Kinematic structure of a wildland fire plume observed by Doppler lidar

A. M. Charland, *San Jose State University*
Craig B. Clements, *San Jose State University*

JOURNAL OF GEOPHYSICAL RESEARCH: ATMOSPHERES, VOL. 118, 3200–3212, doi:10.1002/jgrd.50308, 2013

Kinematic structure of a wildland fire plume observed by Doppler lidar

A. M. Charland[1,2] and C. B. Clements[1]

Received 28 August 2012; revised 19 January 2013; accepted 27 February 2013; published 29 April 2013.

[1] Wildland fires present a challenging environment to make meteorological measurements. Observations in the vicinity of wildland fires are needed to better understand fire-atmosphere interactions and to provide data for the evaluation of coupled fire-atmosphere models. An observational study was conducted during a low-intensity prescribed fire in an area of complex terrain with grass fuels east of San José, California. A ground-based scanning Doppler lidar acquired radial wind velocities and backscatter intensity in and around the fire plume from multiple horizontal and vertical scans. The development of a convergence zone was consistently observed to exist downwind of the plume and was indicated by a decrease in radial velocity of 3–5 m s^{-1}. Divergence calculations made from the lidar radial velocities showed that the magnitude of convergence ranged between -0.06 and -0.08 s^{-1} downwind of the plumes, while a maximum of -0.14 s^{-1} occurred within the plume near the fire front. Increased radial velocities were observed at the plume boundary, indicating fire-induced acceleration of the wind into the base of the convection column above the fire front. Thermodynamic measurements made with radiosondes showed the smoke plume had a potential temperature perturbation of 3.0 to 4.4 K and an increase in water vapor mixing ratio of 0.5 to 1.0 g kg^{-1}. Plume heights determined from sequential range height indicator scans provided estimates of vertical velocity between 0.4 and 0.6 m s^{-1}, representing the ambient background vertical velocity as the top of the plume likely reached equilibrium.

Citation: Charland, A. M., and C. B. Clements (2013), Kinematic structure of a wildland fire plume observed by Doppler lidar, *J. Geophys. Res. Atmos.*, *118*, 3200–3212, doi:10.1002/jgrd.50308.

1. Introduction

[2] While wildland fires are a natural occurrence and promote the health of ecosystems, they can destroy communities around the globe, resulting in high economic costs [*Westerling et al.*, 2006; *Bowman et al.*, 2009]. A key aspect in managing wildfires is improved understanding of the physical mechanisms that drive fire behavior. While advances in understanding wildfire dynamics have been made with the development of coupled fire-atmosphere modeling systems [*Coen et al.*, 2004; *Linn et al.*, 2007; *Mell et al.*, 2007; *Mandel et al.*, 2009], there is a lack of observational data for evaluating these systems. Therefore, high spatial and temporal observations in the vicinity of wildland fires are required to better understand the dynamics of fire-atmosphere interactions and to provide data sets for coupled fire-atmosphere model validation. Because of the difficulty in using in situ instrumentation in the wildland fire environment, remote-sensing instrumentation becomes most practical for both personnel safety and instrument protection since it allows the region around a wildland fire to be probed from a safe distance.

[3] Wildland fires are generally classified as being either wind driven or plume driven. Wind-driven fires are typically fast moving and more predictable than plume-driven fires since the ambient wind is thought to drive their spread. Plume-driven fires, on the other hand, are driven by complex circulations associated with the convection column and can be less predictable since downdrafts can potentially spread the fire in the direction opposite of the ambient wind [*Potter*, 2011]. The behavior of the plume is dependent on winds in the lower 2–3 km of the atmosphere [*Banta et al.*, 1992]. Even during wind-driven fires, plume dynamics are often dominated by strong updrafts generated by buoyancy from the hot gases in the convection column above the combustion zone. The updraft in the plume is subsequently associated with downward motion in other regions of the smoke column that can result in outflow at the surface affecting fire spread [*Banta et al.*, 1992; *Potter*, 2011]. Another recognized dynamic feature of a wildfire plume is the rear inflow, which descends on the upwind side of the fire plume [*Clements et al.*, 2007; *Potter*, 2011]. The rear inflow has been shown to exist in idealized numerical simulations in grass fires [*Sun et al.*, 2009], and *Clark et al.* [1996] suggested that low pressure develops downwind of the fire front, accelerating winds at

[1]Department of Meteorology and Climate Science, San José State University, San José, California, USA.
[2]Now at Dept. of Atmospheric Sciences, University of Utah, Salt Lake City, Utah, 84112, USA.

Corresponding author: C. B. Clements, Department of Meteorology and Climate Science, San José State University, San José, CA 95192, USA. (Craig.Clements@sjsu.edu)

2169-897X/13/10.1002/jgrd.50308

the fire front. They hypothesized that the low pressure forms a convergence zone downwind of the fire since the convection column is advected downwind of the fire front by faster ambient wind speeds aloft tilting the plume downstream and shifting the center of the low-level convergence ahead of the fire. The convergence pattern is responsible for the often observed parabolic shape of the fire line as it draws in low-level air equally from all sides [*Clark et al*., 1996].

[4] To date, there have been limited observations of actual wildland fire plumes and their associated dynamics. One of the most comprehensive field studies to observe the dynamics of a fire plume and associated fire-atmosphere interactions is the FireFlux experiment [*Clements et al*., 2007, 2008; *Clements*, 2010], where a high-intensity, wind-driven head fire was allowed to spread through a suite of tower-based micrometeorological instrumentation. This study observed the turbulent structure of the fire plume and near-surface environment and observed strong downdrafts of ~5 m s^{-1} occurring behind the fire front, in agreement with the modeling results of *Sun et al*. [2009]. While the FireFlux experiment provided evidence of the downward motion behind the fire front, its observations were limited to the two tower locations within the experimental plot. Therefore, the spatial variations in wind fields around fire fronts and plumes are not well observed.

[5] Other studies have used remote-sensing techniques to observe fire-atmosphere dynamics during active wildfires. For example, *Coen et al*. [2004] used infrared imagery to examine the dynamics of a crown fire. The wind field was derived from an infrared imaging camera using image flow analysis techniques. Observations from this study indicated that strong inflow into the base of the convective updrafts occurred. More recently, *Dold and Zinoviev* [2009] used video photography to observe the changes in a light-colored piece of cloth that was tied to vegetation downwind of a fire front to interpret wind fields near a fire front. Observations showed that the cloth was influenced by the winds from the fire as it progressed toward the vegetation. However, it was observed that the cloth was undisturbed by the wind during certain times throughout the burn, indicating a decrease in wind velocity and the potential development of a convergence zone downwind of the fire.

[6] Few studies have been conducted near wildland fires using ground-based remote-sensing measurements; *Banta et al*. [1992] were the first to use a Doppler lidar and a Doppler radar to obtain smoke-column observations from two forest fires. Of the two fires, one was a wildfire, while the other a prescribed burn. During the first forest fire, a pair of counter-rotating horizontal vorticities was observed within the smoke column. The velocity structure of a horizontal plane through the smoke plume showed faster flow existing along the edges of the plume with decreased flow along the centerline. The second fire was observed with the lidar, indicating flow convergence and anticyclonic whole-column rotation. Estimated peak vertical velocities of 15 m s^{-1} were found along with vorticity of approximately 10^{-2} s^{-1}.

[7] In this study, observations of the kinematic structure of a wildland fire plume using a scanning Doppler lidar are analyzed. On 13 July 2011, a prescribed burn was conducted in an area of complex terrain east of San José, California. The paper is organized as follows: The experimental design and a description of the lidar and scanning strategies are described in section 2, results from the analyses of the lidar observations are discussed in section 3, and conclusions are drawn and summarized in section 4.

2. Methodology and Experimental Design

[8] In order to study the wind field around a wildland fire, this experiment capitalized on a prescribed fire conducted in complex terrain. Prescribed fires are controlled burns conducted by fire management agencies to remove fuels in fire-prone areas in order to reduce the risk of wildfires occurring and to restore health to the ecosystems. This prescribed fire provided a unique opportunity to examine the velocity field around a wildland fire and its plume to study fire-induced circulations. A suite of instrumentation was deployed in and around the prescribed burn unit. The instrumentation for this experiment included a scanning pulsed Doppler lidar, a sodar, a micrometeorological tower, two radiosonde systems, and two portable remote automated weather stations (RAWS). The burn unit and instrument placement for the field experiment are shown in Figure 1. The burn unit area, outlined in black, included approximately 660 acres of oak woodland in complex terrain ranging in elevation from 450 to 800 m above sea level. The fire was ignited at 11:43 PST from the northeast corner of the burn unit at the top of the ridge, allowing for the fire to spread slowly downslope as a backing fire, a fire that spreads against the wind. Fire crews continued igniting fire along different lines throughout the day to keep the fire burning down the slope. Due to the sporadic and complex ignition pattern, multiple convection cores were observed throughout the burn. While the ignition pattern was not ideal,

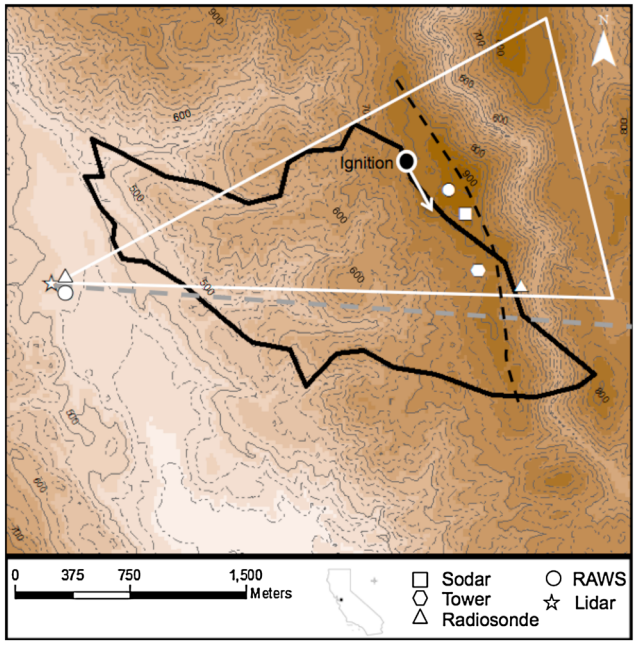

Figure 1. Topographic map of the experimental site showing the burn unit boundaries (outlined in black) and the instrument locations. Darker shading represents higher terrain. Contour interval is 50 m. The black dashed line indicates the location of the ridge. The white outline illustrates the location covered in the horizontal lidar scans, while the grey dashed line shows the location of the vertical lidar scans.

it did provide a unique opportunity to study fire-atmosphere interactions.

[9] On the morning of the burn on an upper-level trough contributed to cloudy conditions with light precipitation that kept the temperature cool, humidity high, and fuels wet. At the site, a moist layer extended from the surface to 500 m above ground level (AGL), as indicated in the radiosonde sounding launched from the valley location at 09:00 PST (Figure 2a). The clouds began to dissipate around 11:00 PST, and the lower boundary layer dried out by 11:49 PST (Figure 2a). During the morning hours, wind speeds in the lower 500 m were between 1 and 3 m s^{-1} and increased to 5 ms^{-1} in upper levels, while the wind direction was mainly from the west (Figure 2b). For the duration of the experiment, the prevailing surface winds were from the west-northwest (Figures 3a and 3b), with more westerly winds along the ridge crest. However, winds observed from the RAWS located to the north of the burn site were more southwesterly and those to the east were more south southeasterly (Figures 3c and 3d). While fuel samples were collected the day before the burn to estimate the fuel moisture and loading, the samples were corrupted during transfer from the site. We therefore estimated the fuel moisture from the *National Wildfire Coordinating Group Fireline Handbook, Appendix B* [*NWCG*, 2006], using an air temperature of 17°C and a relative humidity of 57% taken from the ridge top RAWS at the time of ignition. Average fine dead fuel moisture was estimated at 9%. The estimated fuel loading for grass was 0.12 kg m^{-2} (0.5 tons $acre^{-1}$) taken from the same area during a previous study [*Seto and Clements*, 2011].

2.1. Instrumentation

[10] The remote-sensing instrumentation deployed for this experiment included a pulsed Doppler lidar for radial winds and aerosol backscatter, a Radiometrics, Inc., MP-3000A profiling radiometer for temperature and humidity profiles, and an ASC-4000 miniSoDAR to capture the vertical profiles of wind and turbulence structure. Surface conditions were measured using a micrometeorological tower for high-frequency turbulence measurements within the burn unit and two RAWS for ambient surface conditions. Additionally, two radiosonde systems, a GRAW GmbH & Co. KG GS-E using DFM-06 radiosondes and a Vaisala, Inc., DigiCora MW31 using RS-92GPS radiosondes, obtained temperature and wind profiles upwind from the burn unit in the valley location as well as downwind and within the plume from the ridge top location.

[11] In order to measure ambient surface conditions in the area, one RAWS was placed upwind of the burn area at a lower elevation and another was placed on the ridge top just downwind of the ignition line. Each station was equipped with a Campbell Scientific, Inc., CR1000 data logger, a CS215 temperature and relative humidity probe, and an R.M. Young 5103 prop anemometer. Temperature, relative humidity, and wind speed and direction were averaged over 1 min. A 6.7 m micrometeorological tower was also deployed near the ridge top within the burn unit to obtain high-frequency measurements during the fire front passage. A 3-D sonic anemometer (Sx Probe, Applied Technologies, Inc.) sampled u, v, w velocities and sonic temperature at 10 Hz at 6 m AGL. Total and radiative heat fluxes emitted from the fire as the fire front passed the tower were measured from two Schmidt-Boelter-type heat flux sensors (Hukseflux Thermal Sensors B.V., Model SBG01, Medtherm Corp. Model 64). The sodar was deployed on the ridge downwind of the burn unit to obtain measurements near the plume and ignition line to validate lidar data. Wind speed and direction, in addition to turbulence statistics, were averaged every 10 min from 20 to 200 m in increments of 5 m.

2.2. Lidar Specifications

[12] This study examines the radial velocity and backscatter intensity from a Halo Photonics, Ltd., Stream Line 75 pulsed Doppler lidar. *Pearson et al*. [2009, 2010] provided

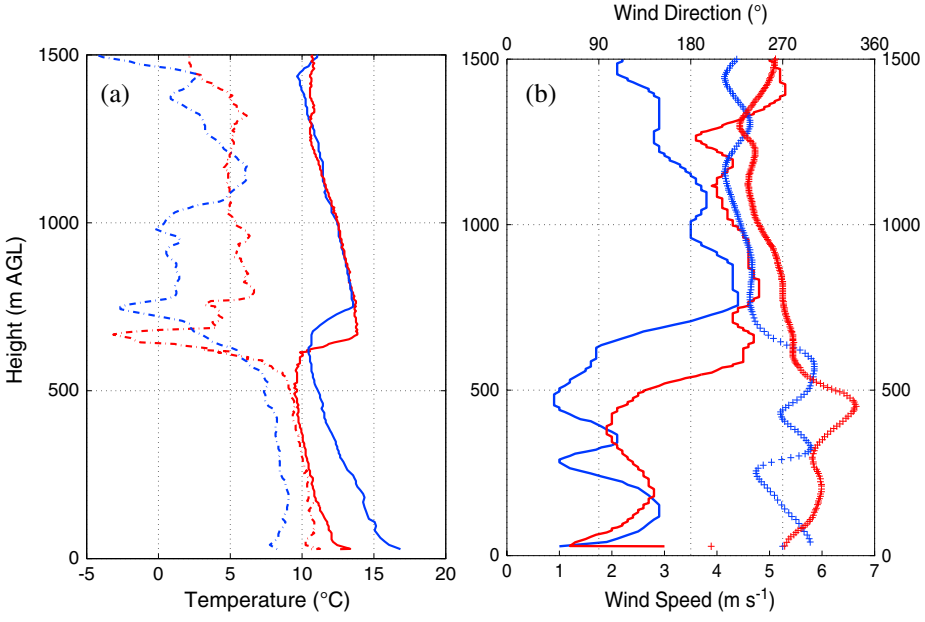

Figure 2. Temperature (solid) and dew point (dashed) temperature profiles (a) and wind speed (solid) and direction (+) profiles (b) from radiosonde soundings at 9:01 PST (red) and 11:49 PST (blue) on 13 July 2011.

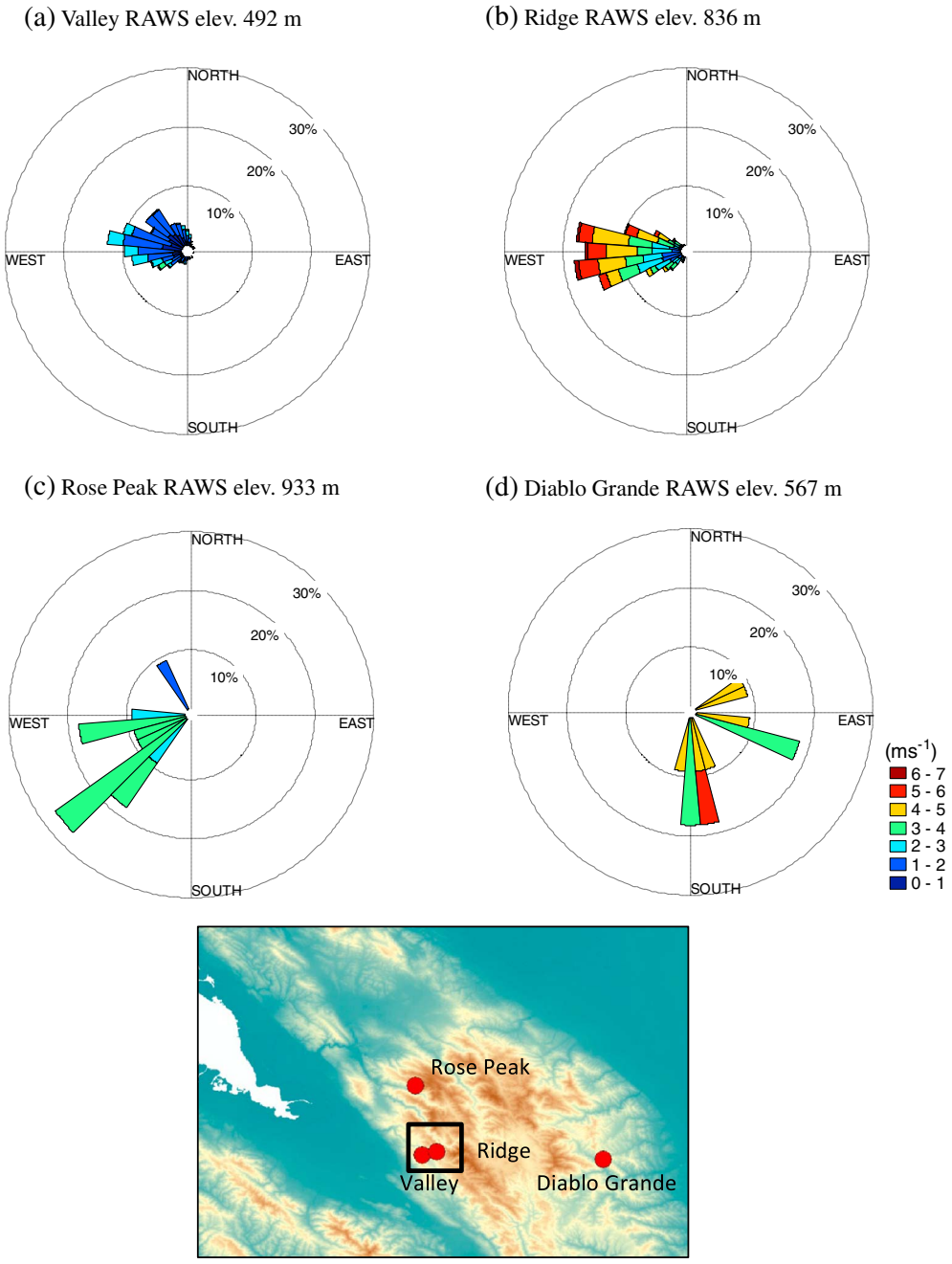

Figure 3. Wind rose plots of wind speed and direction at four RAWS locations (a–d) from 8:00 to 18:00 PST on 13 July 2011. A map showing the location of each station is illustrated, with the black box indicating the experiment area.

a detailed description of the characteristics and performance of the lidar. It emits an eye-safe infrared light at a wavelength of 1.5 μm, which aerosols scatter in the atmosphere. The lidar is equipped with a 75 mm aperture all-sky optical scanner enabling it to scan from 0° to 360° in azimuth angle and from −15° to 195° in elevation angle. There are up to 550 possible user-defined range gates at 24 m spacing with a minimum range of 80 m and the maximum range at 9.6 km. For this experiment, the maximum range was set to 3500 m since the location of the firing operations was within ~1 km of the lidar. Also, a range gate interval of 30 m was used, allowing finer-scale features in the region of the fire to be resolved, which is an improvement over the 300 m resolution from previous studies scanning fire plumes [*Banta et al.*, 1992]. The temporal resolution varied from 0.1 to 180 s, depending on the type of scan scheduled. While scanning a region, the stationarity assumption must be applied. This assumes that the atmosphere does not statistically change over the time it takes to complete a scan [*Stull*, 1988].

[13] The study by *Pearson et al.* [2009] examined the biases and instrumental error of the Halo Photonics lidar by comparing it to other measurement platforms. The analysis of multiple 1 h long records of vertical velocity found minimal biases as all records were within ±2 cm s^{-1} of zero. *Pearson*

et al. [2009] found an estimated error of <10 cm s^{-1} in the atmospheric boundary layer by comparing these records with a 51-day period of vertical velocity measurements. Also, comparisons of wind profiles from the lidar and radiosonde, radar, and anemometer data found very good agreement.

2.2.1. Scanning Strategies and Data Quality Assurance

[14] Different lidar scanning techniques can be applied to study the structure of a smoke plume. The first technique is a stare, which allows for observing the change in the boundary layer height and vertical velocity at one location over time [*Lothon et al*., 2009]. In this technique, the lidar emits a vertically pointed pulse and returns the Doppler radial velocity, which represents the profile of the vertical velocity with height. For this study, a suite of scan schedules was developed in order to have the ability to scan in any direction. A range height indicator (RHI) scan uses a fixed azimuth angle while varying the elevation angle in order to obtain a vertical cross-section through the atmosphere. Plan position indicator (PPI) scans were also performed using a fixed elevation angle while varying azimuth angles to obtain a nearly horizontal cross-section of the atmosphere.

[15] Different methods were used for post-processing the lidar data to correct for instrumental errors. Since the minimum range for the lidar is 80 m, the first step in processing the data was to remove any data within the first 100 m to eliminate any potentially corrupted data. The raw data examined from the lidar also contain fluctuating radial velocity data after a certain point along the beam as the signal is attenuated. The point at which the variance in radial velocity increases along the beam is different for each scan. Therefore, an algorithm was created to determine the location where the difference between two adjacent values of velocity exceeds an unrealistic value. For these cases, the threshold value for this difference was chosen to be ± 7 m s^{-1}, with the assumption that a velocity change of this magnitude within 30 m is unrealistic. Since the radial velocity data beyond this point are considered unrealistic, any backscatter intensity data retrieved are also assumed to be invalid and therefore not used in the analyses.

[16] Depending on the location of the fire, various angles were tested to obtain the best observations in and around the plume. The elevation angle was adjusted for scans to avoid the lidar beam hitting surrounding terrain and to optimize the area of the plume scanned. In this study, an azimuth angle of 95° and elevation angles ranging between 7.5° and 45° in increments of 2.5° were used for the RHI scans. Also, an elevation angle of 10° and azimuth angles ranging from 30° to 70° in increments of 1.0° were used for the PPI scans.

2.2.2. Lidar Data Processing

[17] In order to study the wind field near the fire, the near-edge smoke boundaries of the plume were determined by the backscatter intensity from the lidar scans. Since backscatter intensity can vary greatly in each scan, it is difficult to determine the region of the smoke boundary by using a specific threshold value. *Kovalev et al*. [2005] determined a method for determining the near-edge smoke boundaries from PPI lidar scans. The method determines the boundary by the location of the maximum gradient of the ratio of the backscatter intensity to the integral of the backscatter intensity from the first range gate to the current range gate. The plume boundary was calculated for each azimuth angle and at each range gate following *Kovalev et al*. [2005]:

$$D(r) = \frac{d}{dr}\left[\frac{B(r)}{\int_{r_{\min}}^{r} B(r)dr}\right] \quad (1)$$

where $B(r)$ is the backscatter intensity at range gate r and $r_{\min}$ is the starting range gate. The location of the maximum of $D(r)$ for each azimuth angle indicates the location of the plume boundary for that scan. This algorithm determines the boundary closest to the lidar. This method worked well for finding the zones of multi-layered smoke plumes; however, sometimes the maximum would be found at a location that was not necessarily the edge boundary but at a point within the plume. Similar techniques have also been used for determining cloud height and cloud layers from lidar data [*Pal et al*., 1992; *Chen et al*., 2010].

[18] The *Kovalev et al*. [2005] algorithm works well for the determination of the boundary of an aerosol plume because it eliminates the need for using a criterion value to recognize the difference between the plume and the clear air, which can be dramatically different depending on the intensity of the fire. The end boundary, or downwind edge of the plume, can also be determined using a slight modification to equation (1). Instead of taking the integral from the first range gate, a reverse integral can start from the last range gate and integrate backward to find the boundary at the end of the plume. The accuracy of the end boundary depends on the validity of the lidar data behind the plume. Studies that have determined the cloud top height from lidar data alone have found it difficult to distinguish between the backscatter signal decreasing due to total attenuation within the cloud and that where the top of the cloud is reached. *Venema et al*. [2000] compared lidar and radar measurements of cloud top height to determine if the data were significantly different. The cases where the height differed by ~100 m were determined to be due to total attenuation of the signal. In this study, the validity of the backscatter data within and beyond the plume is determined by the examination of the Doppler radial velocity returned. At a certain range gate the velocity fluctuates due to attenuation of the signal. All the data beyond the range gate where the variance in the velocity is ± 7 m s^{-1} are then considered invalid and removed. Therefore, any boundary that is determined by the algorithm is within the region of valid data. In Figure 4a, the backscatter signal is shown with the peak indicating the smoke plume. The front and end plume boundaries, shown in Figure 4b, indicate that the algorithm was successful in finding the locations both in front of and behind the plume.

3. Results

3.1. Thermodynamic Plume Properties

[19] The thermodynamic properties of the fire front were measured as the fire passed the micrometeorological tower. The total heat flux was measured to determine the intensity of the fire. The total heat flux measured was ~2.5 kW m^{-2} (Figure 5a), indicating a very low intensity fire, indicative of a backing fire. Incident radiative heat flux was less than 0.78 kW m^{-2}, and the near-surface plume temperature measured at 2 m AGL was 51.6°C at the time of the fire front

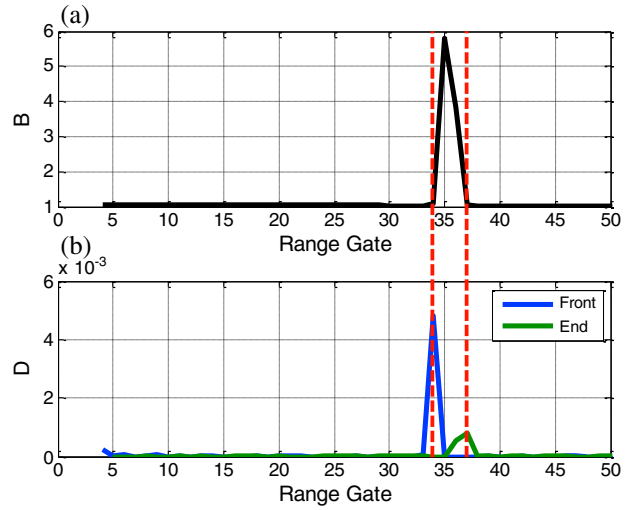

Figure 4. (a) Backscatter intensity (SNR +1) as a function of the range gate. (b) The function $D(r)$ is shown for the front (blue) and end (green) boundaries. The red dashed line indicates that the peak in $D(r)$ occurs at the front and end boundaries of the plume.

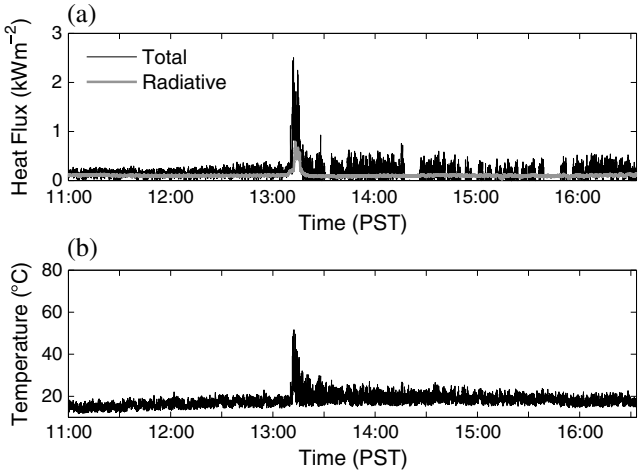

Figure 5. One-second averaged total (black) and radiative (grey) heat fluxes (a) and temperature (b) from the micrometeorological tower within the burn unit on 13 July 2011.

passage (Figure 5b). These values are very low compared to other experimental fires in similar fuels [e.g., *Seto et al.*, 2013]. The reason for this is that the heat flux sensors were mounted at 0.75 m AGL and orientated horizontally such that the plane of the sensor faced perpendicular to the fire front as it slowly burned as a backing fire past the tower. Fuels were removed from the base of the tower by approximately 2 m. Therefore, the very low heat flux measurements do not represent what the fire gave off in the vertical, just what was measured from the side at the tower. From photographs taken during the burn, flame lengths varied from 0.5 m for the low-intensity backing fire fronts to ~10 m for heading fires that were allowed to spread upslope with the wind. Most of the ignition lines were stripping head fires where multiple small strips of fuel (~20 m in width) were burned at the same time. Each fire line was allowed to burn into the already burned area downwind of the preceding fire line.

[20] In order to measure plume properties above the surface, two radiosondes were launched into the plume from a downwind location. At 12:37 PST, a radiosonde was launched so that it ascended through the plume. Due to the location of the plume relative to the balloon launch site, only a very shallow layer of the plume was sampled. The potential temperature at the surface was 298.8 K and decreased to 294.5 K at the top of the plume layer at 80 m AGL (Figure 6a), a perturbation of ~4 K within the plume. The water vapor mixing ratio at the surface was 7 g kg^{-1} and increased by ~1 g kg^{-1} at 80 m AGL before decreasing to ambient. Also, the RAWS at the top of the ridge measured an increase in relative humidity of ~8% (not shown) after the time of ignition. Increased moisture concentration is expected within the plume due to the release of water vapor as a by-product of combustion [*Potter*, 2005]. These measurements are comparable to those found by *Kiefer et al.* [2012], who observed an increase in potential temperature within a wildland fire plume of 3–5 K and a water vapor mixing ratio perturbation of 0.5–3.5 g kg^{-1}. Plume water vapor mixing ratio perturbations of 2 g kg^{-1} were found by *Clements et al.* [2006], which are slightly higher than the observations from this study as a result of the different fuel conditions during the experiments. During the Meteotron fire experiment, the water vapor mixing ratio was estimated to have increased by 1.37 g kg^{-1} due to combustion [*Benech*, 1976].

[21] After the fire moved farther west into the burn unit, another radiosonde was launched into the plume from the top of the ridge (16:44 PST). This radiosonde ascended a slightly deeper layer of the plume relative to 12:37 PST. The top of the plume layer was 259 m AGL as indicated by the warmer potential temperature and increased water vapor mixing ratio. While this is not the plume height, it is the layer that was sampled by the radiosonde. The potential temperature at the surface was 3.5 K warmer than that at 259 m AGL (Figure 6b). The mixing ratio at the surface was 7.8 g kg^{-1} and increased to 8.5 g kg^{-1} at 50 m before decreasing. The enhanced moisture of 0.7 g kg^{-1} above ambient was observed within the plume, and it was less than that observed earlier in the day as the fuels had dried further by the afternoon. At the same time, there was an increase in relative humidity of 7% (not shown) at the RAWS located on the ridge and downwind of the burn area.

3.2. Plume Kinematic Structure

[22] To obtain observations of the kinematic structure within and near the plume, a suite of scanning strategies was scheduled for the lidar. Around 17:00 PST, the fire line moved farther west and closer to the lidar. The observations show that the lidar is able to scan through even the most intense areas of the plume (Figure 7). The regions of high backscatter intensity correspond to areas with high smoke density or the main convection core of the plume. The backscatter intensity is used as a proxy for indicating the location and area of the fire plume. In some scans, there are multiple convection cores observed due to the burn strategies of the fire crews to ignite in multiple lines. While multiple convection cores are commonly observed from a single fire line [*Kiefer et al.*, 2009], the multiple convection cores observed

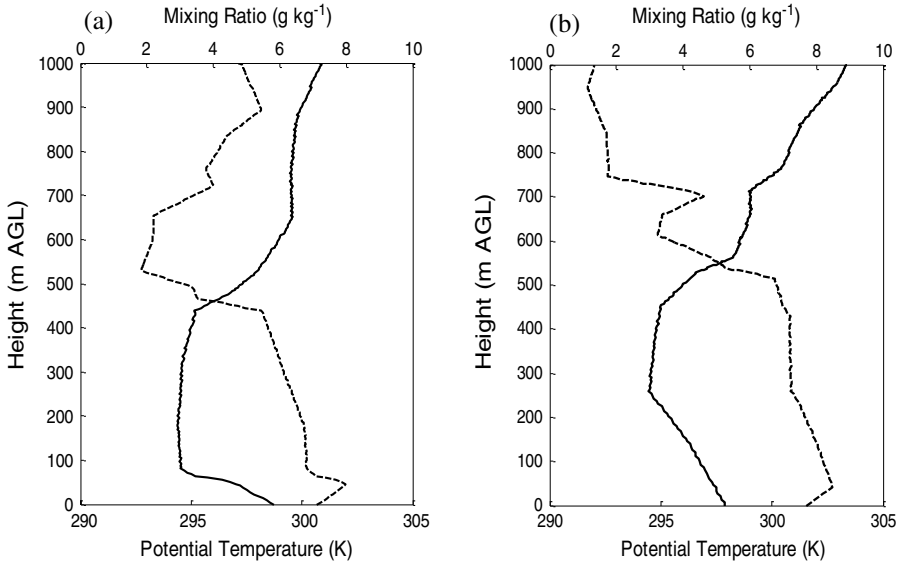

Figure 6. Profiles of water vapor mixing ratio (dashed) and potential temperature (solid) from radiosonde soundings at 12:37 PST (a) and 16:44 PST (b) on 13 July 2011 from the ridge top location released into the plume.

in our case were caused by the burning operations consisting of multiple ignition lines.

[23] To interpret the velocity field obtained from Figure 7, it should be noted that regions of weaker and slightly reversed radial velocities are observed near the 30° azimuth scan angle due to the geometry of the scan. The lidar measures radial velocity along the beam; therefore, with the ambient wind from the northwest, the radial velocity component will be weaker as it is more perpendicular to the ambient wind speed. At approximately 1000 m east and 450 m north of the lidar position (Figure 7a), the scan captures an area of increased radial velocities of ~8 m s^{-1} south of the plume, indicating horizontal acceleration of the wind into the base of the plume near the fire front. Directly downwind of the plume, there is a smaller region of much weaker radial velocities of 0 to 1 m s^{-1}, indicating the formation of a convergence zone. The development of a weak convergence zone downwind of a wind-driven fire front was observed by *Clements et al*. [2007] during the FireFlux experiment. Convergence zones were also observed on a larger scale by *Banta et al*. [1992] during a forest fire. However, *Banta et al*. [1992] observed a reversal in the velocities indicating that a circulation had developed within the plume rather than downwind.

[24] For each PPI scan, the divergence of the radial velocity, δ_r, was calculated from

$$\delta_r = \frac{\partial V_r}{\partial_r} \tag{2}$$

where V_r is the radial velocity and r is the range distance along the lidar beam. At 17:50 PST (Figure 8a), the region of maximum negative divergence, or convergence, of approximately -0.08 s^{-1} corresponds to the location of the convergence zone shown in Figure 7a.

[25] To better determine the magnitude of change of velocities within the convergence zone, the radial velocity along one azimuth angle from the scan that was south of the plume is analyzed (Figure 9a). An acceleration of ~5 m s^{-1} is observed with a sharp decrease of ~3 m s^{-1} along the lidar beam, indicating the location of the convergence zone at 1100 m, which is about 200 m downwind from the main convection core and fire front. In addition, an area of reversed radial velocities between -2 and 0 m s^{-1} is observed to the northeast of the plume, indicating a rear surface inflow into the region of the fire front. A similar magnitude flow reversal was also observed during the FireFlux experiment [*Clements et al*., 2007].

[26] Fire-induced acceleration of the wind into the base of the plume is caused by a horizontal pressure gradient that is created by a low pressure that develops downwind of the fire front and plume [*Smith et al*., 1975; *Kiefer et al*., 2009]. Acceleration of surface winds into the plume base was observed (Figure 7) to occur on both the upwind side and the downwind side, in some instances with a deceleration in velocities downwind of the convection cores. *Coen et al*. [2004] also observed horizontal acceleration into the base of the convective updraft, although on a larger scale, during a wildfire event. The magnitude of the horizontal acceleration was much higher in the study by *Coen et al*. due to the higher intensity of the wildfire that was in forest fuels, which typically burn more intensely given the higher fuel loads.

[27] At 17:52 PST, the convection core progressed to the northwest, with the plume extending toward the southeast (Figure 7b). A similar region of decreased radial velocities was observed downwind of the plume with an adjacent region of increased velocities. The area of convergence had decreased slightly (Figure 8b) but with maximum convergence values around the same magnitude as that observed at 17:50 PST. At 17:55 PST, two convection cores were present (Figure 7c). There is a region south of the larger convection core where velocities increased to 4–6 m s^{-1}, while the region directly downwind and southeast of the plume shows a decrease in velocities of 3–5 m s^{-1}. The region of weaker winds has spread over a larger area than in previous scans, showing an extension of the convergence zone 200 m downwind of the plume; however, the magnitude of the

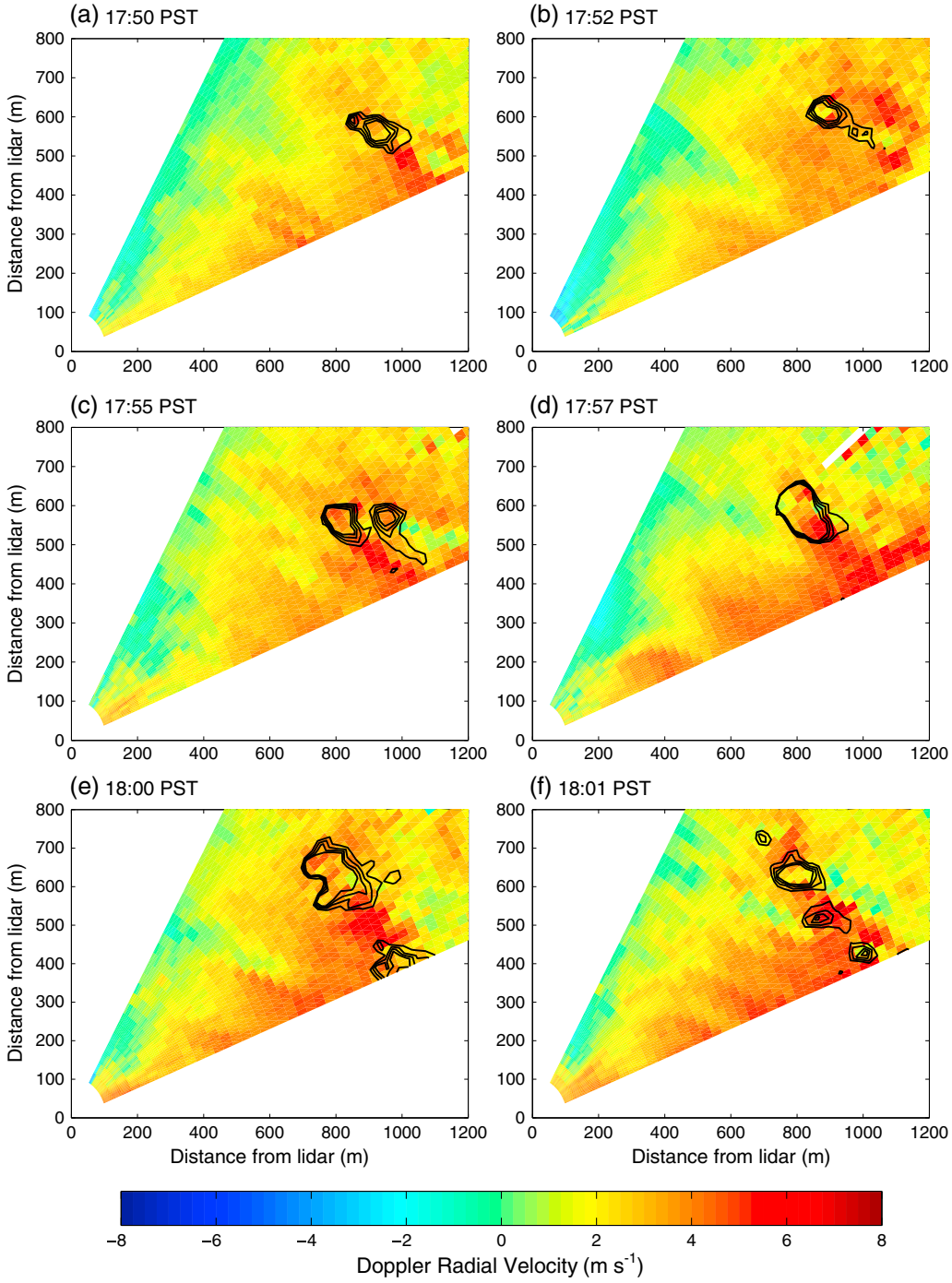

Figure 7. PPI lidar scans of the plume region at specified times with the lidar located at the origin (0,0). An elevation angle of 10° was used with azimuth angles ranging between 30° and 70° in increments of 1.0°. The images show the radial velocity component (m s^{-1}), with the positive values representing flow away from the lidar and negative values representing flow toward it. The black contours outline the areas of high backscatter intensity indicating the location of the plume. Contours are shown from 3.0 to 6.0 by intervals of 1.0 SNR +1.

convergence decreased to 0.06 s^{-1} (Figure 8c). At 17:57 PST, the area of active burning had increased as indicated by the larger area of high backscatter intensity (Figure 7d), which was also confirmed by photography. The region of decreased velocities is still observed downwind; however, the region of accelerated velocities has included a larger area south of the plume. The along-beam velocity shows an increase in radial velocities from 1 to 5 m s^{-1} around 900 m along the beam followed by a sharp decrease in velocities to ~3.5 m s^{-1} around 950 m (Figure 9b). In addition, an area of stronger velocities reaching 8 m s^{-1} was observed in the southeast region of the plume, while weaker velocities between 0 and 2 m s^{-1} were present in the northwest region of the plume. This indicates that the convergence is occurring within the

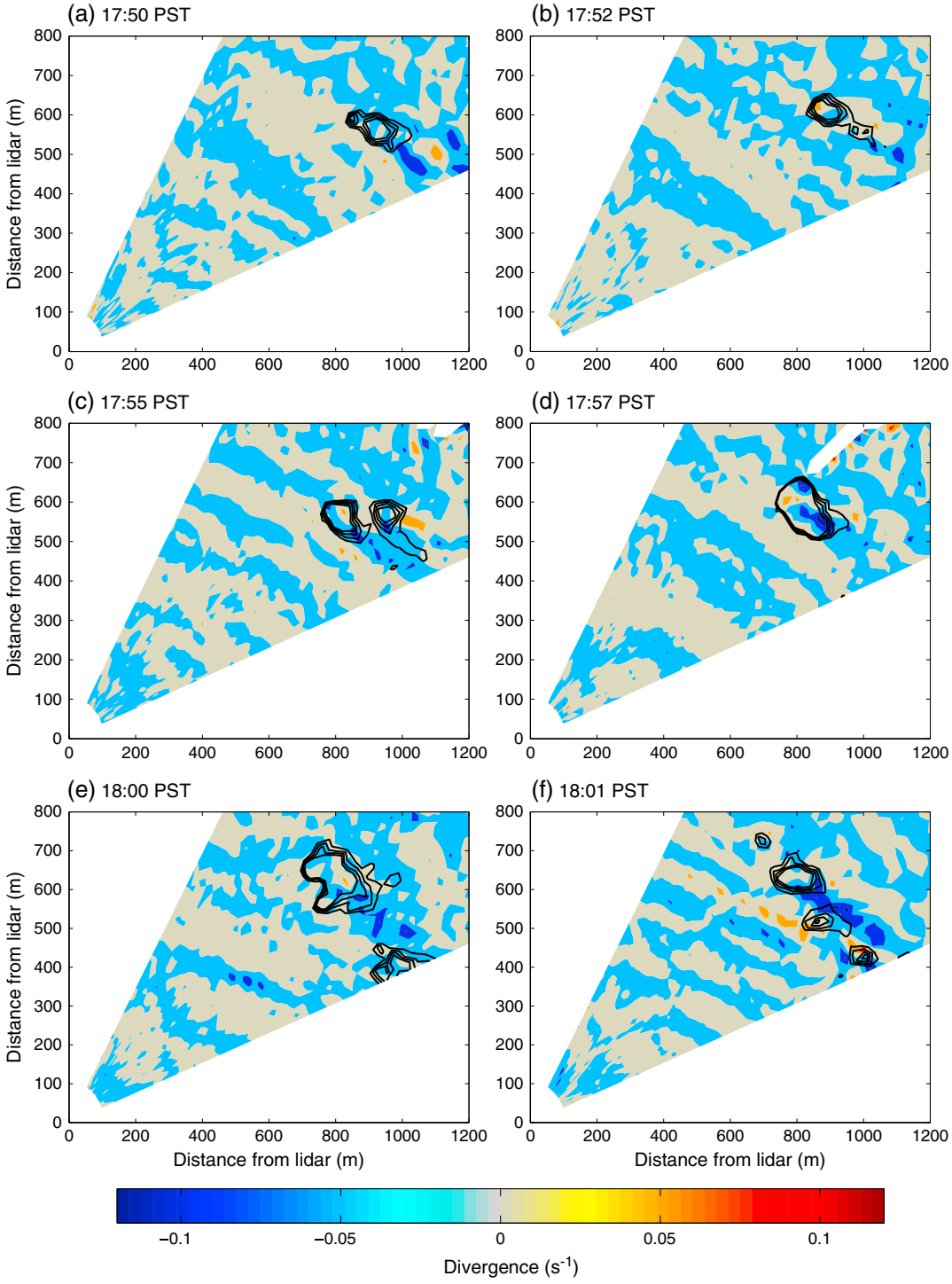

Figure 8. Along-beam divergence calculated from PPI lidar scans. The lidar is located at the origin (0,0). An elevation angle of 10° was used with azimuth angles ranging between 30° and 70° in increments of 1.0°. Positive values represent convergence of the flow, while negative values represent divergence. The black contours outline the areas of high backscatter intensity indicating the location of the plume. Contours are shown from 3.0 to 6.0 by intervals of 1.0 SNR +1.

plume, which is also indicated in Figure 8d with a maximum convergence of -0.14 s^{-1}. *Banta et al.* [1992] also observed a similar structure, but with reversed velocities in the plume, indicating a rotation or vorticity forming within the plume.

[28] At 18:00 PST, fire crews began firing along the southeast region of the burn unit indicated by another region of high backscatter intensity developing near the bottom of the lidar scan (Figure 7e). A convergence zone is observed downwind of the larger convection column by a clearly defined line separating the high and low radial velocities. The radial velocity over the 65° azimuth angle shows a sharp deceleration of the wind from 6 to 1 m s^{-1} within a distance

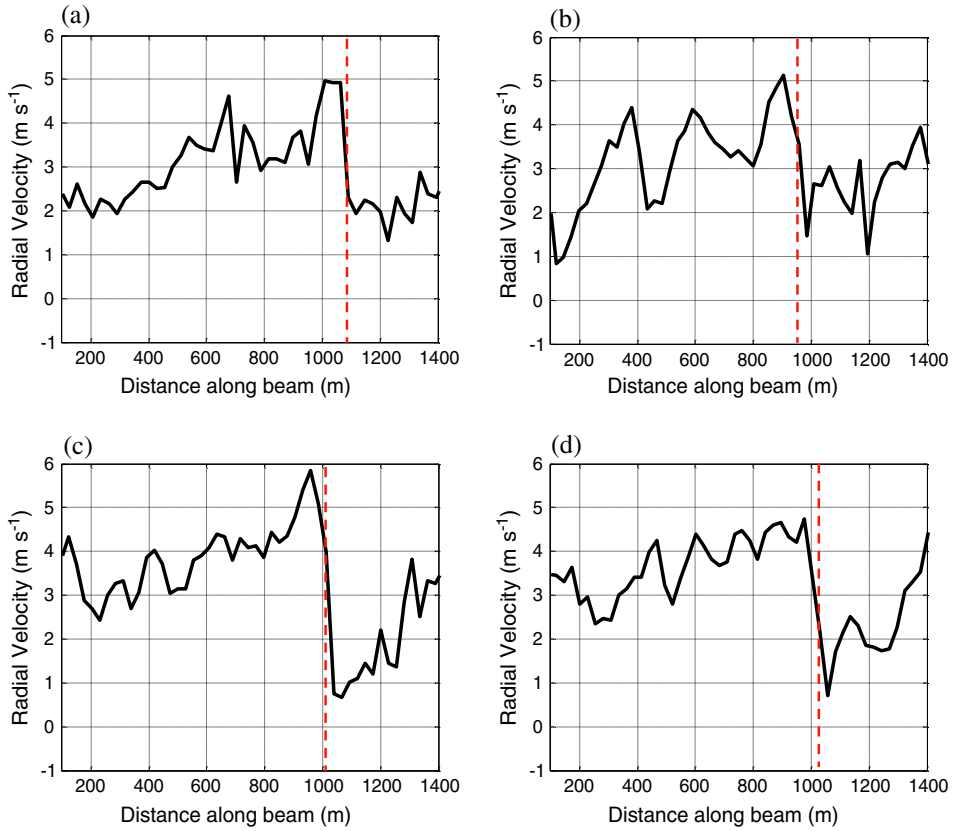

Figure 9. Doppler radial velocities (a) at 17:50 PST on 13 July 2011 for a 10° elevation angle and an azimuth angle of 68°, (b) at 17:57 PST for an azimuth angle of 62°, (c) at 18:00 PST for an azimuth angle of 65°, and (d) at 18:01 PST for an azimuth angle of 64°. The location of the convergence zone is indicated by the red dashed line.

of about 100 m (Figure 9c) and is associated with a strong convergence of -0.11 s^{-1} (Figure 8e). At 18:01 PST, multiple convection columns are observed with several distinct regions of high backscatter intensity (Figure 7f). The decrease in the radial velocity of 4 m s^{-1} is observed at the convergence zone as shown in Figure 9d. The convergence zone again extends downwind of the main convection column parallel with the ambient wind direction (Figure 8f). The consistent presence of the region of weak radial velocities downwind of the convection core indicates that convergence is not transient and most likely plays a major role in the development of near-surface fire-induced circulations that may help drive the fire spread.

[29] In the vertical cross-section scans (RHI) of the plume, there is observed acceleration beneath the plume with weaker velocities aloft (Figures 10a–10d). This indicates a strong indraft into the base of the convection column near the fire front, which has also been observed by *Coen et al*. [2004] and *Kiefer et al*. [2009]. The magnitude of the radial velocity increased as the area of the plume enlarged, indicating that the winds accelerated as the fire spread farther. Velocities at 500 m AGL decreased ahead of the plume and then accelerated in the region of the plume, indicating upper-level divergence (Figure 10a). *Kiefer et al*. [2009] showed that parcels aloft accelerate into the convection column without coming into contact with the heat source of the fire front and suggested that the acceleration is driven by pressure perturbations that develop on the downwind side of the plume. At 17:49 PST, the radial velocities beyond the plume boundary decelerated slightly, which suggests that a region of convergence extended vertically nearly 150 m from the surface to just below the plume (Figure 10b). Deceleration of the flow is also apparent at 18:30 PST, extending 300 m vertically (Figure 10d). The spatial characteristics of the convergence region observed here are similar in scale to those measured by *Banta et al*. [1992], who observed flow convergence of a more intense and larger fire, extending in height to ~1 km above the surface.

[30] Observations from previous studies have identified the location of a near-surface convergence zone ahead of a propagating fire front. *Clements et al*. [2007] observed a short-lived convergence zone ahead of the fire front, while *Banta et al*. [1992] found a convergence pattern downwind related to a downwind line of cumulus congestus clouds that formed. A coupled fire-atmosphere model simulation of grass fires found the convergence pattern to be associated with the downwind tilt of the plume [*Clark et al*., 1996]. Typically, the smoke plume is advected downwind of the fire front, leading to the tilted structure, which results in warmer and rising air ahead of the fire front. *Markowski and Richardson* [2010] suggested that a positive pressure perturbation must exist above a warm bubble (or fire plume) since the rising warm air laterally pushes air above it out of the way, leading to upper-level divergence. As a result, a negative pressure perturbation can develop at the surface, allowing for the formation of flow convergence beneath

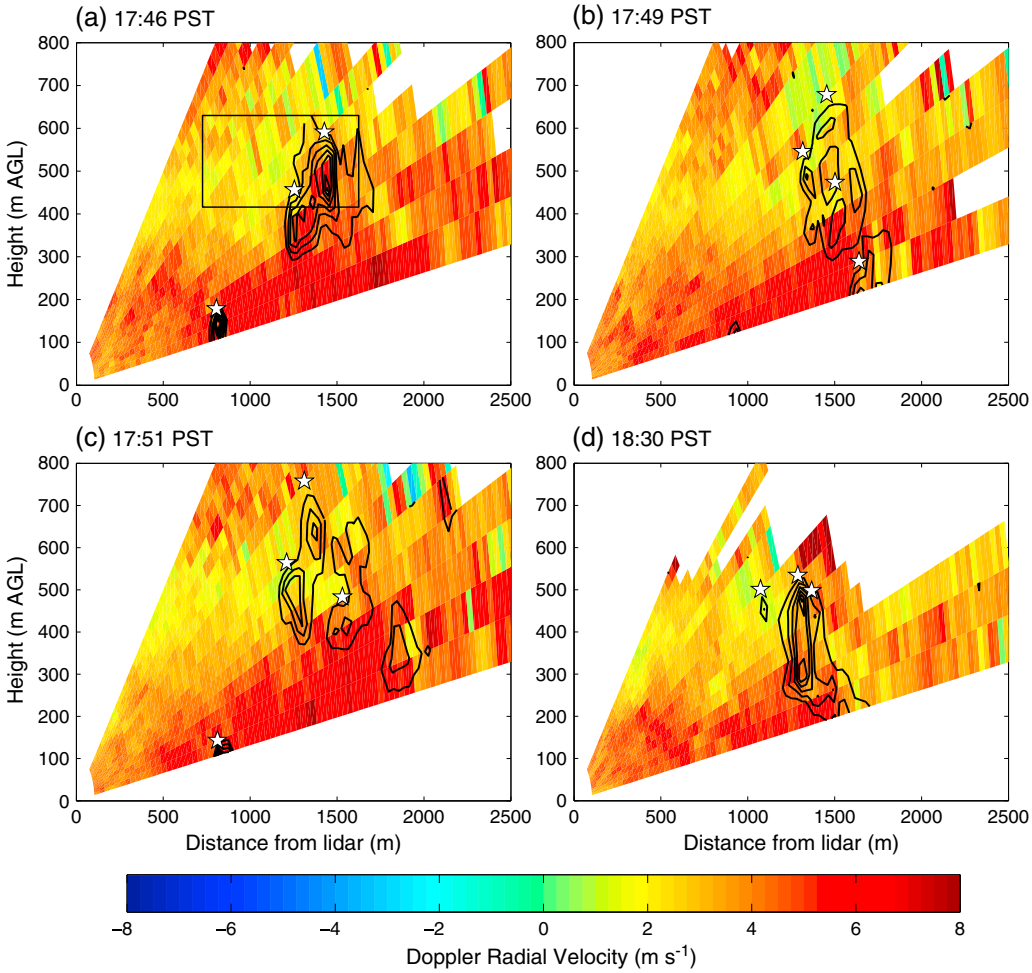

Figure 10. RHI lidar scans of the plume region along a 95° azimuth angle at specified times with the lidar located at the origin (0,0). The images show the radial velocity component (m s^{-1}), with the black contours outlining areas of high backscatter intensity indicating the location of the plume. Contours are shown from 0.0 to 3.0 by intervals of 0.25 SNR +1. The white stars represent the calculated plume height.

the plume. To date, the negative pressure perturbation ahead of a propagating fire front has only been observed once to our knowledge. During a recent pilot study [*Clements et al.*, 2010], a pressure decrease of 0.5 mb was measured at the surface just ahead of a passing fire front. Unfortunately, during this experiment, the surface pressure sensor on the micrometeorological tower failed.

3.3. Plume Height Observations

[31] Plume height determination is important for forecasting many air pollution applications, such as smoke transport and dispersion. The use of a scanning Doppler lidar can provide a higher temporal and spatial resolution measurement of plume height during active wildland fire events than satellite estimates, especially since plume injection heights occur mostly within the atmospheric boundary layer [*Sofiev et al.*, 2012], where ground-based lidars can easily sample. An algorithm similar to equation (1) for determining plume boundaries was used to determine plume height for the RHI scans in Figure 10. In this case, instead of integrating the backscatter intensity across all range gates for a specified azimuth angle, the integral is taken across the elevation angles at a specified range gate. By integrating from a higher elevation angle to a lower one, the height of the plume is identified as the location where the maximum gradient of the backscatter intensity occurs. The calculated plume height for each RHI scan is indicated by white markers in Figures 10a–10d. The algorithm was successful in identifying the location for each range gate of the scan where the maximum gradient of the backscatter intensity occurs. This method for determining plume height is appropriate for examining the vertical extent of the plume and how the plume disperses over time. It should be noted, however, that the RHI scans represent a vertical slice through the tilted plume, and so they do not necessarily represent the maximum height of the plumes measured but do indicate the top of the smoke that was scanned.

[32] At 17:46 PST, the maximum plume height from the lidar scan was 591 m AGL and increased to 678 m after 3 min, indicating little vertical development within the plume (Figures 10a and 10b). The estimated vertical velocity or calculated rate at which the plume rose was 0.48 m s^{-1}. By 17:51 PST, the height increased to 758 m AGL at a rate of 0.66 m s^{-1} (Figure 10c). At 18:30 PST, the plume height decreased to 534 m as the plume dispersed (Figure 10d). The estimated vertical velocities are low compared to other plume measurements [i.e., *Clements et al.*, 2007] and are

considered to represent the ambient background vertical velocities as the top of the plume likely reached equilibrium. The magnitudes are similar to what was measured by the sodar located downwind (not shown). Based on these measurements, the algorithm is able to identify the location where the maximum gradient of the backscatter occurs and provides an estimate for plume rise and vertical velocity.

4. Summary and Conclusions

[33] In this paper, the kinematic structure of a wildland fire plume from a low-intensity prescribed burn was examined with a suite of instruments including a scanning Doppler lidar. Results show that increases of the radial velocities were observed at the plume boundary, indicating acceleration of the wind into the base of the convection column above the fire front. A rear inflow into the fire front was also observed by a reversal of radial velocities upwind the plume. A convergence zone was consistently observed downwind of the plumes. Divergence calculations made from the lidar radial velocities show the magnitude of convergence ranged between -0.06 and $-0.08\ s^{-1}$ downwind of the plumes, while a maximum of $-0.14\ s^{-1}$ occurred within the plume near the fire front. The development of the observed convergence zone is hypothesized to form as a result of the upward motion within the plume causing a negative pressure perturbation at the surface.

[34] An algorithm for determining plume height from sequential RHI scans was tested to estimate plume rise. Plume vertical velocity was estimated between 0.4 and $0.6\ m\ s^{-1}$ and represents the ambient background vertical velocity as the top of the plume likely reached equilibrium. While these measurements do not represent the typical vertical motion of an intense wildfire, they do provide a preliminary assessment of the technique. Further testing of the algorithm is planned on large wildfire events to better gauge its usefulness for wildfire managers.

[35] While our observations do quantify some unique fire-atmosphere interactions associated with a low-intensity prescribed fire and plume, our study does have some limitations that should be noted. In particular, the fuels were not sampled adequately for modeling purposes. In future experiments, a more rigorous sampling of the fuel conditions will be conducted to better characterize the fuels and resulting fire behavior. Also, the fire ignition patterns were far from ideal, making it difficult to determine where the fire was at any given time. The use of airborne video would provide a better means to document the fire line evolution required for modeling studies. In addition, the lidar scanning techniques that were used can be adjusted in future work to obtain a better temporal resolution than that obtained during this study. With a smaller range gate and continuous scanning, it will be possible to measure finer details of the plume structure and calculate turbulence statistics from the lidar observations. Also, this prescribed fire was conducted in conditions leading to a fairly low intensity fire. In the future, the lidar will be mounted in a truck bed, allowing for quick deployment to active wildfires. In addition, using scans at a faster temporal resolution will improve the analysis of the motions within the plume. Also, the lidar can only examine the convergence along radial velocity, limiting the analysis to one component of the wind; however, the winds converge into a fire column from all sides. Future studies could use dual-Doppler lidar scanning strategies to examine multiple components of the convergence around the fire and to allow for better analysis of the kinematic structure of a fire plume.

[36] **Acknowledgments.** This work has been supported by research grants from the National Science Foundation (AGS-0960300) and the USDA (07-JV-11242300-073). We also acknowledge the Santa Clara County Parks for special use permit 12046. We thank Battalion Chief Dave McLean and firefighters from the Cal Fire Santa Clara Unit for accommodating our research objectives during their prescribed burn. We also thank Daisuke Seto, Dianne Hall, and Richard Bagley for helping with the experimental setup.

References

Banta, R. M., L. D. Oliver, E. T. Holloway, R. A. Kropfli, B. W. Bartram, R. E. Cupp, and M. J. Post (1992), Smoke-column observations from two forest fires using Doppler lidar and Doppler radar, *J. Appl. Meteorol.*, *31*, 1328–1349.

Benech, B. (1976), Experimental study of an artificial convective plume initiated from the ground, *J. Appl. Meteorol.*, *15*, 127–137.

Bowman, D. M. J. S., et al. (2009), Fire in the earth system, *Science*, *324*, 481–484, doi:10.1126/science.1163886.

Chen, Z., W. Liu, Y. Ahang, J. He, J. Ruan, S. Li, and Y. Cui (2010), Study on the cloud layer height and properties in Hefei observed by lidar, 5th International Symposium on Advanced Opitcal Manufacturing and Testing Technologies, 6 pp.

Clark, T. L., M. A. Jenkins, J. Coen, and D. Packham (1996), A coupled atmosphere-fire model: convective feedback on fire-line dynamics, *J. Appl. Meteorol.*, *35*, 875–901.

Clements, C. B., B. E. Potter, and S. Zhong (2006), In-situ measurements of water vapor, heat, and CO2 fluxes within a prescribed grass fire, *Int. J. Wildland Fire.*, *15*(3), 299–306, doi:10.5194/acp-10-5891-2010.

Clements, C. B., et al. (2007), Observing the dynamics of wildland grass fires: FireFlux- a field validation experiment, *Bul. Amer. Meteorol. Soc.*, *88*, 1369–1382, doi:10.1175/BAMS-88-9-1369.

Clements, C. B., S. Zhong, X. Bian, W. E. Heilman, and D. W. Byun (2008), First observations of turbulence generated by grass fires, *J. Geophys. Res.*, *113*, D22102, doi:10.1029/2008JD010014.

Clements, C. B. (2010), Thermodynamic structure of a grass fire plume, *Int. J. of Wildland Fire*, *19*, 895–902, doi:10.1071/WF09009.

Clements, C. B., D. Seto, and W. Heilman (2010), The grass fires on slopes experiment, Eos Trans. AGU, Fall Meet. Suppl., Abstract NH41A-1483.

Coen, J., S. Mahalingam, and J. Daily (2004), Infrared imagery of crown-fire dynamics during FROSTFIRE, *J. Appl. Meteoro.*, *43*, 1241–1259, doi:http://dx.doi.org/10.1175/1520-0450(2004)043<1241:IIOCDD>2.0.CO;2.

Dold, J. W., and A. Zinoviev (2009), Fire eruption through intensity and spread rate interaction mediated by flow attachment, *Combust. Theor. and Model.*, *13*, 763–793, doi:10.1080/13647830902977570.

Kiefer, C. M., C. B. Clements, and B. E. Potter (2012), Application of a mini Unmanned Aircraft System for in situ monitoring of fire plume thermodynamic properties, *J. Atmos. Ocean. Tech.*, *29*, 309–315, doi:http://dx.doi.org/10.1175/JTECH-D-11-00112.1.

Kiefer, M. T., M. D. Parker, and J. J. Charney (2009), Regimes of dry convection above wildfires: idealized numerical simulations and dimensional analysis, *J. Atmos. Sci.*, *66*, 806–836, doi:10.1175/2008JAS2896.1.

Kovalev, V. S., J. Newton, C. Wold, and W. M. Hao (2005), Simple algorithm to determine the near-edge smoke boundaries with scanning lidar, *Appl. Optics*, *44*, 1761–1768, doi:http://dx.doi.org/10.1364/AO.44.001761.

Linn, R. R., J. L. Winterkamp, C. Edminster, J. J. Colman, and W. S. Smith (2007), Coupled influences of topography and wind on wildland fire behavior, *Int. J. Wildland Fire*, *16*, 183–195, doi:10.1080/13647830902977570.

Lothon, M., D. H. Lenschow, and S. D. Mayor (2009), Doppler lidar measurements of vertical velocity spectra in the convective planetary boundary layer, *Bound-Lay. Meteorol.*, *132*, 205–226, doi:10.1007/s10546-009-9398-y.

Mandel, J., J. D. Beezley, J. L. Coen, and M. Kim (2009), Data Assimilation for Wildland Fires: Ensemble Kalman filters in coupled atmosphere-surface models, *IEEE Control Syst. Mag.*, *29*, 47–65, doi:10.1109/MCS.2009.932224.

Markowski, P., and Y. Richardson (2010), Mesoscale meteorology in mid-latitudes, Wiley-Blackwell, 407 pp.

Mell, W., M. A. Jenkins, J. Gould, and P. Cheney (2007), A physics-based approach to modeling grassland fires, *Int. J. Wildland Fire*, *16*, 1–22, doi:10.1071/WF06002.

National Wildfire Coordinating Group (2006), Fireline Handbook, PMS 410–2.

Pal, S. R., W. Steinbrecht, and A. I. Carswell (1992), Automated method for lidar determination of cloud-base height and vertical extent, *Appl. Opt.*, *31*, 1488–1494.

Pearson, G., F. Davies, and C. Collier (2009), An analysis of the performance of the UFAM pulsed Doppler lidar for observing the boundary layer, *J. of Atmos. And Oceanic Tech.*, *26*, 240–250, doi:10.1175/2008JTECHA1128.1.

Pearson, G., F. Davies, and C. Collier (2010), Remote sensing of the tropical rain forest boundary layer using pulsed Doppler lidar, *J. Atmos. Chem. Phys.*, *10*, 5891–5901, doi:10.5194/acp-10-5891-2010.

Potter, B. E. (2011), Effects of complex terrain on extreme fire behavior, synthesis of knowledge of extreme fire behavior: Volume I for Fire Managers, PNW-GTR-854, USDA.

Seto, D., C. B. Clements, and W. E. Heilman (2013), Turbulence spectra measured during fire front passage, *Agr. Forest. Meteorol.*, *169*, 195–210, doi:10.1016/j.agrformet.2012.09.015.

Seto, D., and C. B. Clements (2011), Fire Whirl Evolution Observed during a Valley Wind-Sea Breeze Reversal, *J. Combust.*, *13*, doi:10.1155/2011/569475.

Smith, R. K., B. R. Morton, and L. M. Leslie (1975), The role of dynamic pressure in generating fire wind, *J. Fluid Mec.*, *68*(1), 1–19.

Sofiev, M., T. Ermakova, and R. Vankevich (2012), Evaluation of the smoke-injection height from wild-land fires using remote-sensing data, *J. Atmos. Chem. Phys.*, *12*, 1995–2006, doi:10.5194/acp-12-1995-2012.

Stull, R. B. (1988), An Introduction to Boundary Layer Meteorology, 666 pp., Kluwer Academic Publishers, Dordrecht, The Netherlands.

Sun, R., S. K. Krueger, M. Jenkins, A. Zulauf, and J. J. Charney (2009), The importance of fire–atmosphere coupling and boundary-layer turbulence to wildfire spread, *Int. J. Wildland Fire*, *8*, 50–60, doi:10.5194/acp-12-1995-2012.

Venema, V., H. Russchenberg, A. Apituley, A. van Lammeren, and L. Ligthart (2000), Cloud boundary height measurements using lidar and radar, *Phys. Chem. Earth*, *25*, 129–134.

Westerling, A. L., H. G. Hidalgo, D. R. Cayan, and T. W. Swetnam (2006), Warming and earlier spring increase western U.S. forest wildfire activity, *Science*, *313*, 940–943, doi:10.5194/acp-12-1995-2012.